Received: 5 August 2021 | Revised: 8 June 2022 | Accepted: 18 July 2022

DOI: 10.1002/esp.5457

RESEARCH ARTICLE

ESPL WILEY

# Combined seismic and borehole investigation of the deep granite weathering structure—Santa Gracia Reserve case in Chile

Rahmantara Trichandi[1,2] | Klaus Bauer[1] | Trond Ryberg[1] | Dirk Scherler[1,3] | Klaus Bataille[4] | Charlotte M. Krawczyk[1,2]

[1]GFZ German Research Centre for Geosciences, Potsdam, Germany

[2]Technische Universität Berlin, Berlin, Germany

[3]Freie Universität Berlin, Berlin, Germany

[4]University of Concepción, Concepción, Chile

**Correspondence**
Rahmantara Trichandi, GFZ German Research Centre for Geosciences, Telegrafenberg, 14473 Potsdam, Germany.
Email: chandi@gfz-potsdam.de

**Funding information**
German Science Foundation (DFG) priority research programme SPP-1803 'EarthShape: Earth Surface Shaping by Biota', Grant/Award Number: KR 2073/5-1

## Abstract

Imaging the critical zone at depth, where intact bedrock transforms into regolith, is critical in understanding the interaction between geological and biological processes. We acquired a 500 m-long near-surface seismic profile to investigate the weathering structure in the Santa Gracia National Reserve, Chile, which is located in a granitic environment in an arid climate. Data processing comprised the combination of two seismic approaches: (1) body wave tomography and (2) multichannel analysis of surface wave (MASW) with Bayesian inversion. This allowed us to derive P-wave and S-wave velocity models down to 90 and 70 m depth, respectively. By calibrating the seismic results with those from an 87 m-deep borehole that is crossed by the profile. We identified the boundaries of saprolite, weathered bedrock, and bedrock. These divisions are indicated in the seismic velocity variations and refer to weathering effects at depth. The thereby determined weathering front in the borehole location can be traced down to 30 m depth. The modelled lateral extent of the weathering front, however, cannot be described by an established weathering front model. The discrepancies suggest a more complex interaction between different aspects such as precipitation and topography in controlling the weathering front depth.

**KEYWORDS**
borehole, geophysics, Bayesian inversion, body wave tomography, critical zone, geomorphology, geophysics, Rayleigh wave, regolith, seismic survey, surface wave tomography, velocity gradient, weathering front

## 1 | INTRODUCTION

The interaction between geological, chemical, and biological processes plays an important role in forming the Earth's surface. For example, tectonic uplift exposes bedrock at the surface and allows water- and biota-assisted weathering processes to dissolve rock or transform its structure and composition (Brantley et al., 2007). After disintegration, erosion processes can then remove sediment and expose fresh bedrock from depth. The material that exists, and the collection of geological, chemical, and biological interactions that occur, at the surface and in the shallow subsurface, make up the so-called critical zone (Figure 1). The vertical extent to which the bedrock is actively transforming into weathered bedrock is called the weathering front. Previous studies of weathering in different climates observed the weathering front at different depths (Bazilevskaya et al., 2013; Brantley et al., 2017; Hayes et al., 2020; Stierman & Healy, 1984; Vázquez et al., 2016).

Different weathering processes create porosity and permeability, which itself influences water flow through the rock and thus further influences the dissolution of minerals from the bedrock (Graham et al., 2010). To fully understand how the different processes interact, it is crucial to know the critical zone structure, including the thickness of the regolith layer. To investigate the critical zone structure, direct measurement approaches are often used, based on artificial outcrops,

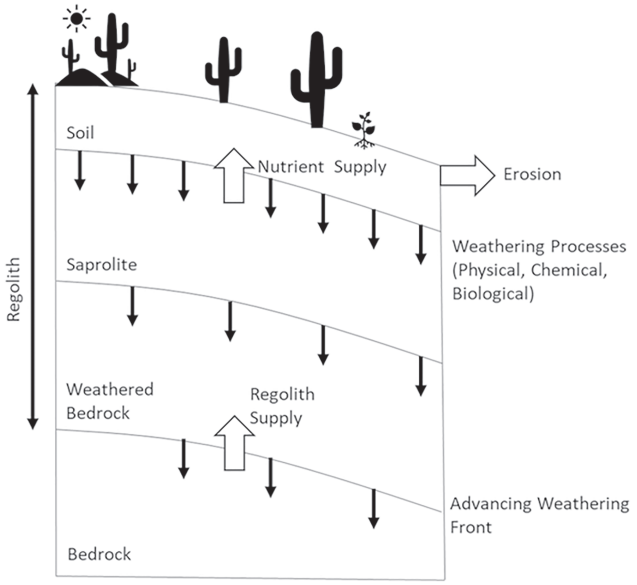


**FIGURE 1** Conceptual illustration of the critical zone structure in an eroding landscape. Soil, saprolite, and weathered bedrock comprise the regolith, which rests on top of the unweathered bedrock. Erosion at the surface allows the weathering front to advance to greater depth with time

soil pits, or borehole cores. While such approaches may yield highly accurate 1D data of the critical zone structure, they commonly provide only limited extent and depth penetration. In addition, while borehole coring and logging can reach down to greater depth, it is typically relatively expensive. Therefore, 2D measurements are needed to spatially sample the heterogeneity across a region (Callahan et al., 2020).

Geophysical approaches such as the seismic method are often used to provide 2D information on the subsurface without altering the subsurface environment. Geophysical methods offer an indirect investigation of rock properties in the subsurface by performing measurements on the surface. Information on rock properties is generally derived from P- and S-wave velocity data, as they are affected by the rock density, porosity, and mineralogy (Befus et al., 2011; Holbrook et al., 2019). In the critical zone, weathered rocks will show significantly lower P- and S-wave velocities values compared to the unweathered bedrock at depth, due to higher porosity, lower density, or the transformation of minerals during the weathering processes.

Different types of rock layers can be identified based on the different P- and S-waves velocities. The P-wave velocity model is commonly produced using body wave tomography, in which arrival times of P-waves are identified to infer the rock's P-wave velocity (e.g. Baumann-Wilke et al., 2012; Befus et al., 2011; Flinchum et al., 2018). As it travels faster than any other waves, the P-wave arrivals can easily be determined in the seismogram as the first impulse recorded. However, this is not the case with S-wave arrivals, as other wave types often superimpose the incoming S-waves. This superimposition creates a problem in producing a shear wave velocity model, especially for shallow targets. Therefore, shear wave velocity models are increasingly built from surface wave data from active seismic sources (Comina et al., 2017; Ivanov et al., 2006; Miller et al., 1999; Park et al., 2005). Previous studies have also shown that producing a shear wave velocity model from surface wave inversion can help to image and identify weathering zones, by their low velocities (Keifer et al., 2019; Wang et al., 2019; Yaede et al., 2015).

The Chilean Santa Gracia Reserve is one of the four focus sites in the EarthShape research priority programme (Dal Bo et al., 2019; Oeser & Von Blanckenburg, 2020; Oeser et al., 2018) that studies the effects of different weathering processes in different climate and environments. The reserve is located in a granodioritic environment with little precipitation and low vegetation cover. In this setting, we expect a relatively shallow regolith depth due to the limited precipitation (Braun et al., 2016; Hayes et al., 2020; Vázquez et al., 2016). Previous geophysical investigations using ground penetrating radar (GPR) could not fully image the critical zone structure as the penetration down to 3 m depth did not reach the bedrock (Dal Bo et al., 2019). We thus aim to image the critical zone in Santa Gracia using body wave tomography and multichannel analysis of surface waves (MASW) methods. We use body wave tomography to create a P-wave velocity model, and MASW, combined with transdimensional Bayesian inversion, to produce an S-wave velocity model. Integrating the P- and S-wave velocity models with existing borehole information enables us to create a conceptual model of the weathering structure in Santa Gracia Reserve. We discuss our results in conjunction with existing borehole logging (Weckmann et al., 2020) and geochemical analysis (Krone et al., 2021) to present an integrated interpretation of the weathering structure. Finally, we compare our results with existing established models of weathering front advances.

## 2 | STUDY SITE AND GEOLOGIC SETTING

The Santa Gracia Reserve is located northeast of La Serena, Chile (Figure 2a). It is located in a transitional area between the arid and semi-arid climatic zones. The mean annual precipitation is 77 mm/year, and the mean annual temperature is 15°C (Karger et al., 2017). The semi-arid climate in this area creates a relatively low vegetation coverage of 30–40% (Bernhard et al., 2018; Oeser & Von Blanckenburg, 2020), dominated by cacti and shrubs sustained by fog. Regional geological data indicates coastal uplift rates of $0.2 \pm 0.1$ mm/year (Kukowski & Oncken, 2006). The regional geological map shows that the reserve is located in an intrusion (130–110 Ma) with a younger intrusion (100–97 Ma) east of the study area (modified from Gobierno de Chile Servicio Nacional de Geologia y Mineria, 2003).

Geologically, the study area is composed of tonalities, diorites, monzodiorites, granodiorites, and monzongranites (Gobierno de Chile Servicio Nacional de Geologia y Mineria, 2003). Some hydrothermal alteration can also be found west of the study area (Figure 2a). Soil pit information from previous studies found that clastic rocks with a 2 mm grain size characterize the upper 0.3 m of the subsurface, while below, more fractured blocks with 5–20 cm size prevail (Bernhard et al., 2018; Oeser et al., 2018). Previous geophysical investigation using GPR imaged the saprolite layer down to 3 m depth (Dal Bo et al., 2019). In Figure 2b, we present a shaded topography map with the seismic profile (red line) and borehole location plotted. The study area is located in a relatively flat area, as shown in the seismic profile topography in Figure 2d, with topographic variation of ~15 m at most.

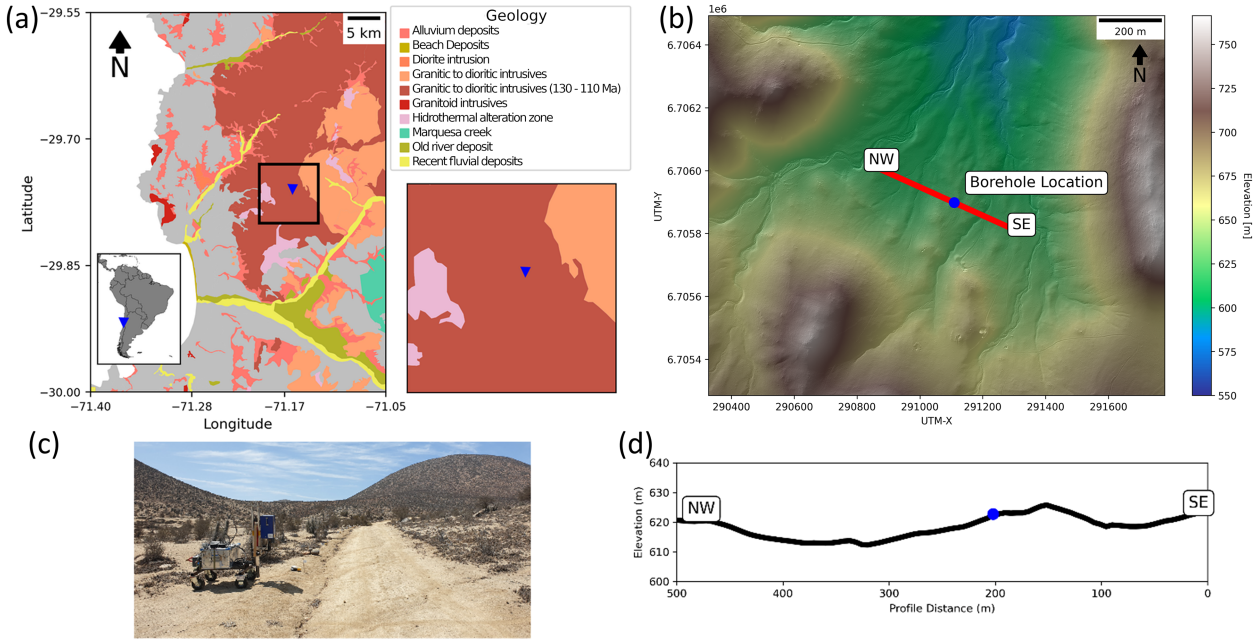


**FIGURE 2** Overview of the study area: (a) regional geological map showing the dominance of granitic rock in the study area (after Gobierno de Chile Servicio Nacional de Geologia y Mineria, 2003); (b) shaded topography map with the locations of the seismic profile (red line) and borehole (blue dot); (c) photo of the seismic survey showing the seismic weight drop source used; and (d) topography of the seismic profile also showing the borehole's location (blue dot) [Color figure can be viewed at wileyonlinelibrary.com]

As part of the EarthShape research programme, a borehole was drilled in 2019, which is located along the seismic profile. Core analysis suggests different zones in the subsurface down to 87 m depth (Krone et al., 2021). Geophysical logging provides P- and S-wave sonic logs and borehole televiewer data (Weckmann et al., 2020). Unfortunately, the P- and S-wave sonic logs provided data from 17 to 87.5 m depth with the upper 17 m of the logging data missing, due to acquisition problems. This part of the borehole is crucial as it covers the depth range where we expected to have the strongest weathering.

### 2.1 | Seismic data acquisition

In January 2020, active seismic acquisition was conducted in the Santa Gracia National Reserve, Chile. A 500 m-long seismic profile was surveyed along a dirt road to image the deep weathering structure around the borehole location (Figure 2b). The elevation varies between 610 and 625 m along the line (Figure 2d). The acquisition parameters were designed to allow for the application of body wave tomography and surface wave analysis. To provide sufficient energy, seismic waves were generated using a 40 kg accelerated weight drop source (Figure 2c). Altogether 135 shot locations were distributed along the profile with shot spacings of 4 m. The shots were recorded by a constant receiver spread of 90 channels deployed with 6 m spacings along the entire line. For each receiver point, we plant a three-component geophone with a 4.5–150 Hz response which is connected to an autonomous CUBE data logger. The connected CUBEs then saved all the data transmitted from the geophone, which will then be individually extracted from each CUBE. The source and receiver locations along the line were projected onto a straight line using the approach of Zelt (1999). Source–receiver offsets remain unchanged in this procedure. Maximum source–receiver offsets vary between 250 and 500 m.

## 3 | METHODOLOGY

### 3.1 | Body wave tomography

Seismic tomography using body waves is a well-established method for imaging near-surface weathering (e.g. Befus et al., 2011; Flinchum et al., 2018; Holbrook et al., 2014; Leone et al., 2020). Similar to the latter mentioned authors, we use first-arrival P-wave travel time tomography to determine the P-wave velocity structure. Noteworthy is that no clear S-wave arrivals could be identified in the weight drop-generated data to run a complementary S-wave travel time tomography since the weight drop source is excited mainly by P-waves and surface waves. For this reason, instead, the surface waves were used to image S-wave velocities.

### 3.2 | Inversion of travel time data

First-arrival travel times were first picked in a receiver gather seismogram, where for a given receiver, the trace recordings from all shots are plotted over the source–receiver offset. An example is shown in Figure 3a. Receiver gathers were chosen instead of shot gathers because of the slightly denser trace spacing (4 m in receiver gathers compared to 6 m in shot gathers), enhancing the continuity of the first-arrival phase. Bandpass filtering (Butterworth, 20–100 Hz) was applied to improve the quality of signals at larger distances. Approximately 8500 travel times were picked in all available receiver gathers.

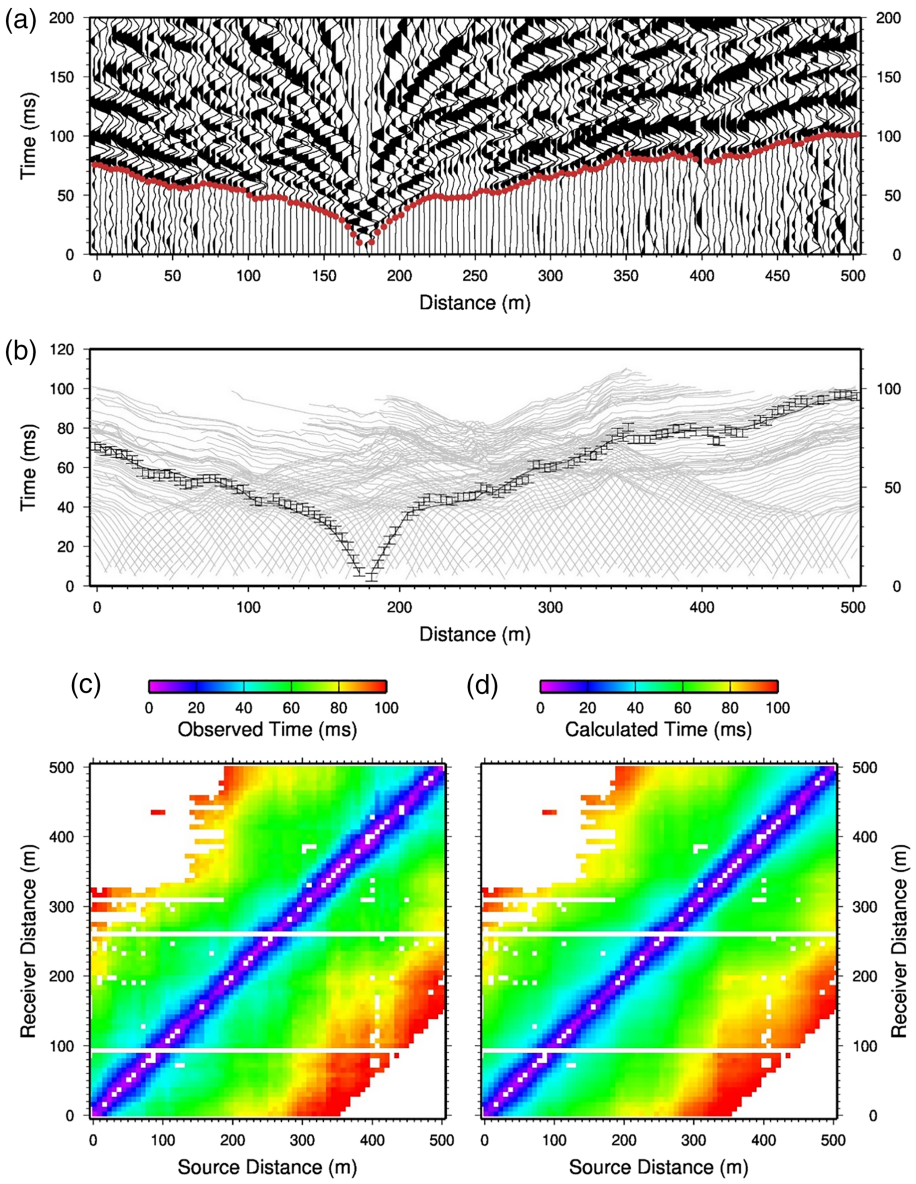


**FIGURE 3** Tomographic inversion approach: (a) exemplary seismogram section showing receiver-gathered traces for all shots recorded by a given receiver, red dots indicate the picked travel times of the first-arrival P-wave; (b) observed picks with error bars and calculated travel times (black line) for one receiver gather, grey lines indicate travel times for all other receiver locations; (c) observed travel times for all picks as a function of source and receiver location; (d) calculated travel times using the final tomographic model [Color figure can be viewed at wileyonlinelibrary.com]

Additional quality control was undertaken by inspecting the picked travel times within the alternative shot-gathered presentation of the data and picks. Based on the comparison of reverse observations, we estimate travel time uncertainties of about 2.5 ms. A starting model for the tomographic inversion was developed using the RAYINVR package (Zelt & Smith, 1992). As a result, a 2D layered velocity structure was established. The root mean square (RMS) misfit between observed and calculated travel times was reduced during the RAYINVR inverse modelling down to about 10 ms.

The subsequent tomographic inversion was carried out using the SIMUL2000 package (Thurber & Eberhart-Phillips, 1999). This iterative method is based on ray tracing and a damped least-squares inversion algorithm. Although SIMUL2000 was initially developed for crustal studies using mainly local earthquake data, it can also be applied to controlled-source data sets and near-surface investigations (e.g. Baumann-Wilke et al., 2012). The grid-based tomographic starting model was generated from the 2D layered RAYINVR model using horizontal and vertical node spacings of 10 and 3 m, respectively. Then, iterative inversion was carried out until the RMS misfit reached values on the order of magnitude of the estimated picking uncertainties. This approach is essential to avoid over-fitting of erroneous data and related potential introduction of artifacts. An example of individual data fitting after the tomographic inversion is shown in Figure 3c. A generally good agreement between observed (Figure 3c) and calculated (Figure 3d) travel times for all picked source–receiver pairs indicates that the tomographic model can explain many details of the measured data. The final model has an RMS misfit of 2.5 ms.

## 3.3 | Multichannel analysis of surface waves

MASW is commonly used to model near-surface S-wave velocity (Konstantaki et al., 2015; Olona et al., 2010; Park et al., 1999; Yaede et al., 2015). Using the MASW method, we extracted the frequency-dependent phase velocity dispersion curves. The dispersion curves were then inverted using a Bayesian approach to produce a 1D S-wave velocity model for observation points along the profile. With multiple 1D S-wave velocity models, we can build a pseudo-2D S-wave velocity profile.

For the seismic data acquired with a weight drop source, we expect the dominant surface wave to be the Rayleigh wave composed

of compressional and vertical particle motion along the surface. Therefore, these specific particle motions are best observed in the vertical component of the seismic data. For this reason, we processed the vertical component of the measured seismic data.

### 3.4 | Extraction of dispersion curves

To extract the Rayleigh wave's phase velocity dispersion curves, we follow the surface-wave dispersion inversion and profiling (SWIP) described by Pasquet and Bodet (2017). Figure 4a shows an example of how we window the seismic data for dispersion stacking for the observation point ($X_{mid}$) located at 205 m in our profile. The steps are as follows:

1. *Selection of traces*. We first select the seismic data trace to be included in our dispersion analysis by creating a receiver window ($L$) around the mid-point ($X_{mid}$). In this example, we used a symmetrical receiver window of 50 m, spanning from $X_{mid} - L/2$ to $X_{mid} + L/2$. Every trace from the receiver located inside this window will be included for the dispersion analysis of the corresponding $X_{mid}$. In Figure 4a, the included receivers are represented by blue inverted triangles.
2. *Selection of shots*. We then select the shots ($FFID$) to be included in the dispersion analysis by determining a shot window ($dS$). For each end of our receiver window, we included shots located inside the range of $X_{mid} - L/2$ to $X_{mid} - L/2 - dS$ and from $X_{mid} + L/2$ to $X_{mid} + L/2 + dS$, respectively. For the example in Figure 4a, we used a shot window of 30 m, and the red squares represent the included shots.
3. *Extraction of shot gathers*. For the next step, we extracted the selected shot gather using the receivers and shots included in steps 1 and 2. An example of a shot gather from $X_{mid} = 205$ m and $FFID = 254$ is shown in Figure 4b. For this specific example, we then collected all 11 shot gathers.
4. *Frequency–phase velocity domain transformation*. For each extracted shot gather, we then transformed it to the equivalent frequency–phase velocity domain to produce a dispersion image. We performed this transformation by using the tools provided in the GEOPSY package (Wathelet et al., 2020).
5. *Selection and stacking of dispersion image*. After the transformation of each shot gather, we then select the dispersion image to be stacked manually to increase the dispersion image quality. An example of the stacked dispersion image of $X_{mid} = 205$ m is shown in Figure 4c.

These processes are repeated for every $X_{mid}$ in our profile, which we sample every 8 m so that we have sufficient changes in the shot and receiver combination.

Finally, we picked the dispersion curve in the frequency–phase velocity domain for each stacked dispersion image. An example of a stacked dispersion image for $X_{mid} = 205$ m is shown in Figure 4c. In this figure, the picked dispersion curve is marked by the blue line. The first step of the dispersion curves picking process was to automatically pick the maximum amplitude for each frequency. After the automatic determination of the dispersion curves, we manually picked the fundamental mode dispersion curve while also filtering the frequency points which contained low amplitude as suggested in the SWIP method (Pasquet & Bodet, 2017). With this workflow, we ensured that the dispersion curve picking is consistent with the maximum amplitude while also avoiding higher mode dispersion. The picking procedure was then repeated for every stacked dispersion image. The picked dispersion curves were then used for the 1D S-wave velocity inversion.

### 3.5 | Bayesian inversion of dispersion curves

To reconstruct the 1D S-wave velocity from the dispersion curves, we implement the transdimensional Bayesian inversion routine described

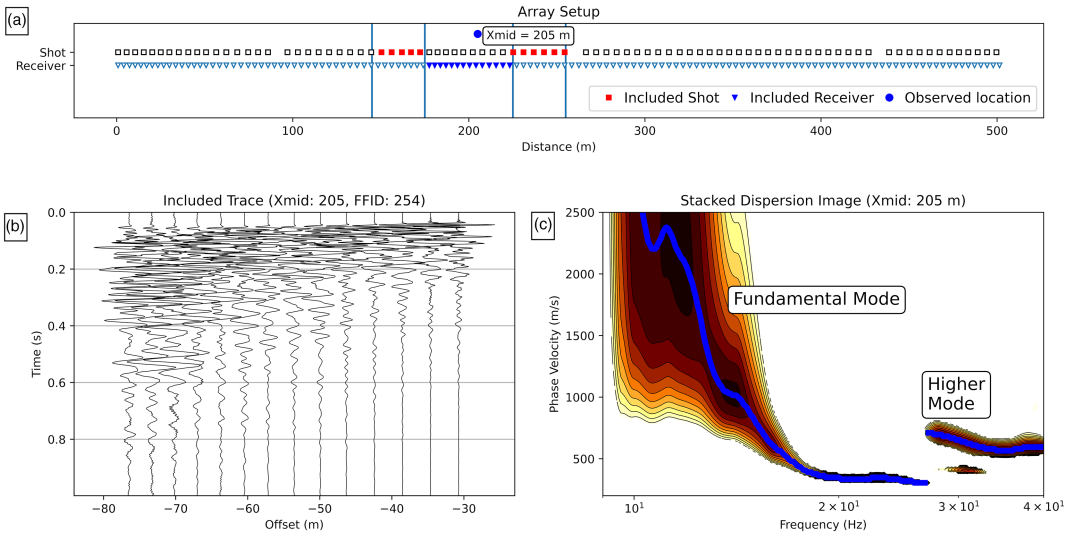


**FIGURE 4** Example of Rayleigh wave's phase velocity dispersion curve extraction process at mid-point ($X_{mid}$) 205 m: (a) geometry used for processing at $X_{mid} = 205$ m, red squares show the included shots and blue inverted triangles show the included receivers; (b) example of a single-shot gather (time – offset) from a source located at 254 m using the geometry from (a); (c) stacked dispersion image for $X_{mid} = 205$ m using the geometry from (a), blue lines represent the Rayleigh wave's phase velocity dispersion curves of different modes [Color figure can be viewed at wileyonlinelibrary.com]

by Bodin (2010). One of the advantages of using this algorithm is that we require only minimal initial information of the real model, for example, the number of layers and each layer's thickness (Ryberg & Haberland, 2019). These parameters will be derived during the inversion by the data itself (data-driven). Additionally, with the trans-dimensional inversion, we need not provide a fixed number of layers as the inversion scheme will also look for the number of layers by adding and reducing the number of layers in the model, according to the data noise level.

The general workflow of the inversion steps (Figure 5) can be summarized as follows. We used the dispersion curve as the input data ($d_{obs}$) and provided a range of values as prior information for the forward modelling parameters. For the initial information, we set a range of values for parameters required for the forward modelling: (i) number of layers $P(N)$; (ii) Voronoi cell location $P(C)$; (iii) data noise $P(\sigma)$; (iv) $P(V_s)$ and $P(V_p)$ value of each Voronoi cell. A random initial model $m_0$ is then generated. For $n$ number of layers in $m_0$, each layer as defined by the Voronoi cell location will have $V_s$ and $V_p$, which is then used for the forward modelling of the dispersion curves. We used the modelling tools from the GEOPSY package (Wathelet et al., 2020). General steps for a chain of Bayesian inversion are as follows:

1. Generate a random starting model ($m_0$) using initial information $P(V_s)$, $P(N)$, $P(C)$, $P(V_p/V_s)$, and $P(\sigma)$.
2. Generate a perturbed model $m_1$ by randomly performing one of the following:

a. Perturb the data noise ($\sigma$) value.
b. Perturb the cell location of a random cell. Changes in the Voronoi cell location will affect the layer's thickness of the input model.
c. Perturb the $V_s$ value of a random cell.
d. Perturb the $V_p/V_s$ value of a random cell and calculate $V_p$ accordingly for the input model.
e. Delete a random cell.
f. Add a random cell according to the prior information provided by the chain.

g. Calculate the acceptance probability ($\alpha$) of moving from $m_0$ to $m_1$ based on the $d_{obs}$, modelled dispersion curve of $m_0$, and modelled dispersion curve of $m_1$.
h. Randomly accept or reject the move from $m_0$ to $m_1$ based on the acceptance probability calculated in step 3. If accepted, $m_0$ is then replaced by $m_1$.
i. Repeat from step 2 until the predetermined number of iterations is reached.

For the inversion, we perform multiple chains of Bayesian inversion for a single input of data $d_{obs}$. The final 1D model is then derived using all the models from all chains.

As previously mentioned, the advantage of using the trans-dimensional Bayesian inversion is that we need only minimum initial information. For all the inversion routines, we provided uniformly distributed initial values on $P(V_s)$, $P(N)$, $P(C)$, $P(\sigma)$, and $P(V_p)$. These are as follows: 0.1–5.0 km/s for $P(V_s)$; 2–20 layers for $P(N)$; 0–100 m for $P(C)$; 0.01–0.30 km/s for $P(\sigma)$, and 0.3–8.0 km/s for $P(V_p)$. We also perform the inversion independent of any information either from the available borehole data or the body wave tomography model.

## 4 | RESULTS

### 4.1 | P-wave velocity model

The final P-wave velocity model for the Santa Gracia critical zone is displayed in Figure 6a. We use a vertical exaggeration of 2:1 to improve the clarity of the image. In general, the areas close to the surface can be modelled with higher reliability than deeper parts. The

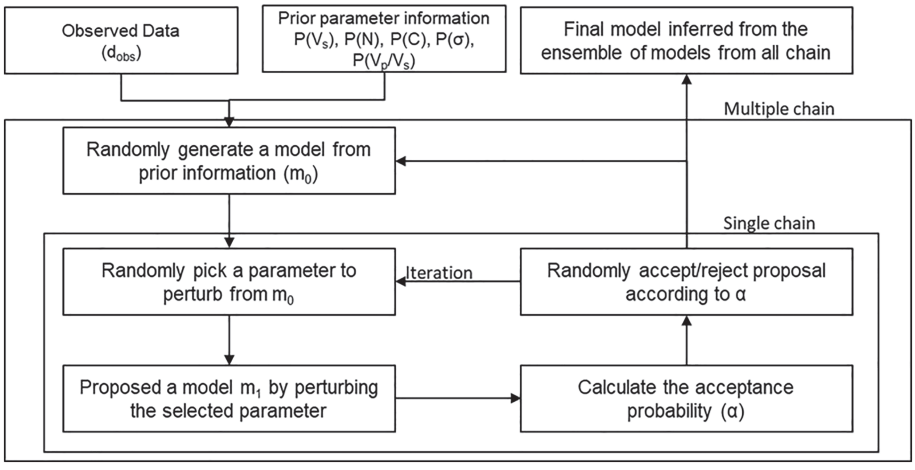


**FIGURE 5** General workflow of the transdimensional Bayesian inversion. Input data $d_{obs}$ is the extracted Rayleigh wave dispersion curve. We give minimum prior information on the expected probability of shear wave velocity value $P(V_s)$, the number of layers $P(N)$, Voronoi cell's location $P(C)$, data noise $P(\sigma)$, and $V_p/V_s$ ratio $P(V_p/V_s)$. The information is then used to generate a starting model $m_0$ for a single chain. A randomly picked parameter from $m_0$ is then perturbed to create a proposed model $m_1$. Both $m_0$ and $m_1$ are then used to calculate the acceptance probability ($\alpha$). Based on $\alpha$, the proposed model $m_1$ is then randomly accepted or rejected. If accepted, we take the proposed model $m_1$ as the initial model $m_0$ in the next iteration. Multiple chains of these processes can be independently run, in which, from all the calculated chains, a final model is then inferred. The model is then limited to the top of the halfspace layer inferred during the 1D inversion of the dispersion curve. The resulting final $V_s$ model is then used to create a pseudo-2D $V_s$ profile by performing linear interpolation and Gaussian smoothing across the profile

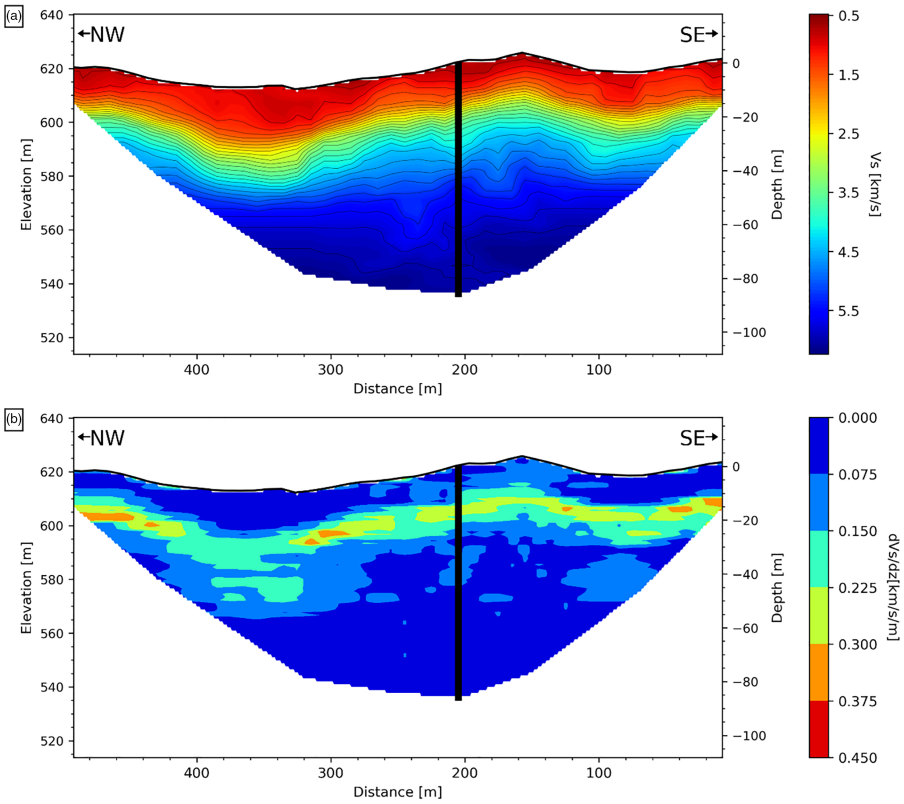


**FIGURE 6** P-wave velocity model at Santa Gracia: (a) smoothed model resulting from tomographic inversion of first-arrival travel times; (b) vertical P-wave velocity gradient illustrating changes of velocity with depth. The vertical black line at 205 m distance indicates the location of the borehole. Models are shown with vertical exaggeration (VE) of 2:1 [Color figure can be viewed at wileyonlinelibrary.com]

model is muted at the edges and for deeper parts where no information on velocity can be derived because of insufficient ray coverage.

To first order, the velocity model indicates a layered structure that runs, with some minor deviations, parallel to the surface topography. The uppermost layer shows P-wave velocities ~0.8 km/s near the surface, increasing to 2–2.5 km/s around 20 m depth. This low-velocity layer appears slightly thicker in regions of local topographic lows, that is, at distances 50–110 and 320–400 m along the profile. Velocities of 2.5–4.5 km/s occur at around 20–40 m depth. At greater depth, we observe velocities reaching values of 4.5–6 km/s. In this deeper layer, contour lines reveal an interesting feature, with lowered velocities and a slight dip encountered around 65–75 m depth at the location of the borehole (vertical line at 205 m distance). The subdivision into three layers is not very sharp and is rather transitional. To enhance more subtle differences in the layered structures, we show the vertical velocity gradient (e.g. Bauer et al., 2010) in Figure 6b. This representation highlights the strong velocity increase with depth, particularly in the range of 10–30 m. The geological meaning of the layers and dipping features will be discussed in the context of the borehole data and the S-wave velocity structure from surface wave analysis.

## 4.2 | S-wave velocity model

The results of the MASW are presented in Figure 7. The S-wave velocity profile is shown in Figure 7a and the vertical S-wave velocity gradient is displayed in Figure 7b. We muted the bottom part of the model, where the depth is primarily defined by a 1D halfspace of the phase velocity modelling. The selection of the halfspace boundary was done automatically by inferring the highest probability of the halfspace during inversion. In addition to the halfspace muting, we also present the standard deviation contour line of 0.2 km/s (the dashed black line in Figure 7a) as recommended in the SWIP approach (Pasquet & Bodet, 2017). While the standard deviation threshold provides a more robust and conservative assumption on the resolution, we consider it is still useful to show the model down to the halfspace boundary limit.

For the S-wave velocity profile, we observe values between 0.38 and 3.10 km/s. We see only slight lateral variations, especially in the upper 30 m, as the horizontal trend of the S-wave velocity contour lines is relatively parallel to the surface topography. Below 30 m depth, we can see some horizontal variations, especially below topographic lows around 300–400 m distance and 50–150 m distance (Figure 7). In these parts of the profile, we observe the deepening of the S-wave velocity contour.

Vertically, we observe a thick, low S-wave velocity layer in the upper part of the profile. This low-velocity feature goes down to ~20 m. Below this thick, low-velocity zone, we observe a high increase in velocity as indicated by the high-velocity gradient (Figure 7b). Finally, we have the relatively constant high-velocity zone of our profile underlying the low-velocity layer.

Like the vertical P-wave velocity gradient model (Figure 6b), the vertical S-wave velocity gradient model in Figure 7b enhances subtle details not apparent in the S-wave velocity model. A high vertical velocity gradient shows an area with strongly varying material properties (heterogenous), while low values represent relatively homogenous material. In the vertical velocity gradient model, we have a top layer with a low gradient followed by a layer with a steep gradient. Similar to the P-wave vertical velocity gradient model, the shape of the strong gradient layer is also relatively parallel with the surface topography. Underlain by a layer with a high vertical velocity gradient, we have another layer with relatively low vertical velocity gradient values.

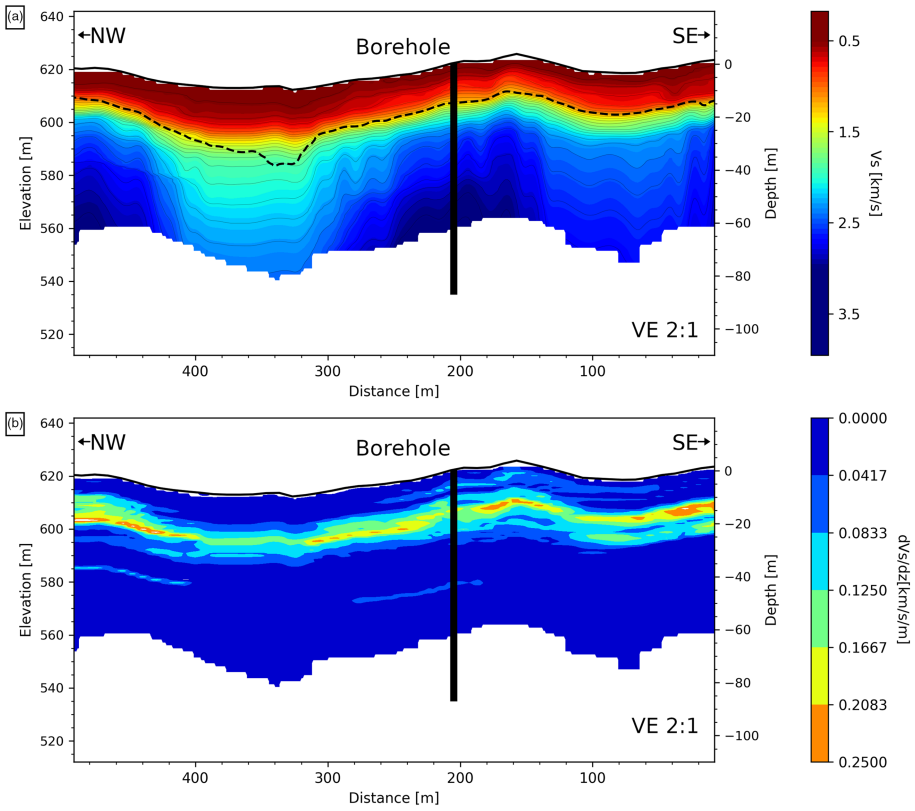


**FIGURE 7** S-wave velocity model at Santa Gracia: (a) smoothed 2D S-wave velocity model derived from surface wave tomography; (b) vertical S-wave velocity gradient derived from (a). Models are shown with vertical exaggeration (VE) of 2:1. Dashed black line in (a) represents the 0.2 km/s standard deviation boundary from the generated models [Color figure can be viewed at wileyonlinelibrary.com]

### 4.3 | $V_p/V_s$ model

With the availability of both P- and S-wave velocity information, it is common to combine both data sets to produce a $V_p/V_s$ profile (e.g. Wadas et al., 2020). However, here we need to consider the different methods and approaches in determining the seismic velocity. The MASW method created a pseudo-2D profile by combining multiple 1D S-wave velocity profiles reconstructed by modelling frequency-dependent phase velocity dispersion curves. In contrast, the body wave tomography method reconstructed the 2D P-wave velocity profile by modelling of ray paths travelling from source to receiver (Pasquet et al., 2015). With the different approaches and sensitivities, we therefore expect a certain degree of incompatibility that can make non-typical $V_p/V_s$ ratios difficult to interpret reliably. We present the $V_p/V_s$ ratio model in Figure 8. While the colour pattern presents interesting isolated high $V_p/V_s$ ratios at the top layer of the topographic lows, we can see that the range of $V_p/V_s$ ratios does not present typical values (>1.73 for unconsolidated rock). A thorough $V_p/V_s$ interpretation requires information on rock petrology, such as porosity, saturation, bulk, and shear modulus (Brantut & David, 2019), which is unavailable for our data set. Because it is beyond the scope of this study to include modelling of these petrophysical parameters, we concentrate on the combined interpretation of the $V_p$ and $V_s$ model across the profile.

## 5 | DISCUSSION

The P- and S-wave velocity information provided by both the body wave tomography and MASW methods provides different perspectives on the critical zone structure in Santa Gracia. Here, we focus on the first-order information provided by these two approaches and integrate them with data from an existing borehole (Krone et al., 2021; Weckmann et al., 2020) to interpret the weathering zone from the surface down to 90 m depth at the borehole location, and then extend it to the entire profile with the obtained 2D seismic data.

### 5.1 | Borehole data confirmation

We integrate the P- and S-wave velocity models with existing borehole information (Weckmann et al., 2020). The borehole is located at distance 205 m from the profile (Figure 9). The borehole information contains televiewer and sonic log data, which we can use to confirm and correlate with the P- and S-wave velocity models.

The televiewer data in Figure 9a shows acoustic amplitudes which are correlated with rock quality. Weathered and fractured rocks return low acoustic televiewer amplitudes. In the uppermost section of the televiewer profile in Figure 9a, we observe low amplitudes between 7 and 30 m depth. Below 30 m depth, we mainly observe high televiewer amplitude. We also encounter another layer with low televiewer amplitude between 72 and 82 m depth in the deeper part of the section. The variability in the televiewer amplitude shows that in the borehole we encounter rocks with differing hardness. The relatively lower amplitude in the upper 30 m shows that the rock in this depth range is relatively weaker compared to the rocks below 30 m depth. The low televiewer amplitudes between 72 and 82 m depth also indicate a relatively weakened rock.

The velocity comparison in Figure 9b shows the S-wave velocity from the MASW (blue) and the sonic log (grey), as well as the P-wave velocity from the body wave tomography (green) and its corresponding sonic log (orange). Due to the weak rock encountered in the upper 20 m below the surface, the sonic log could not be used to determine seismic velocities at this shallow depth range. Using both

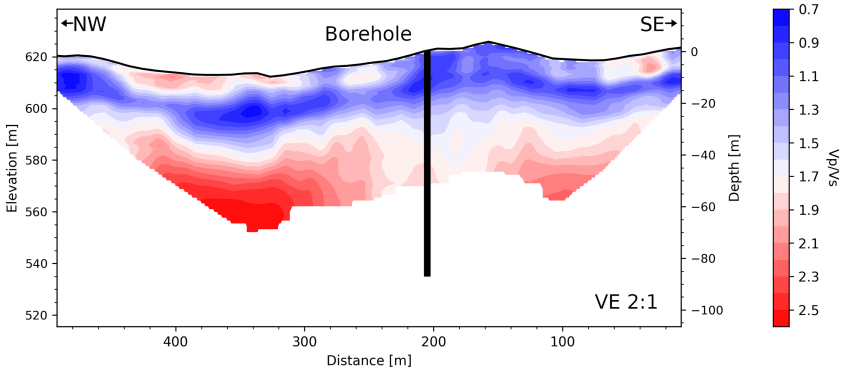


**FIGURE 8** $V_p/V_s$ model produced using the P-wave velocity model from body wave tomography and the S-wave velocity model from the MASW method. The different methods in modelling the P- and S-wave velocity presents a sensitivity problem which disables interpretation of the $V_p/V_s$ model [Color figure can be viewed at wileyonlinelibrary.com]

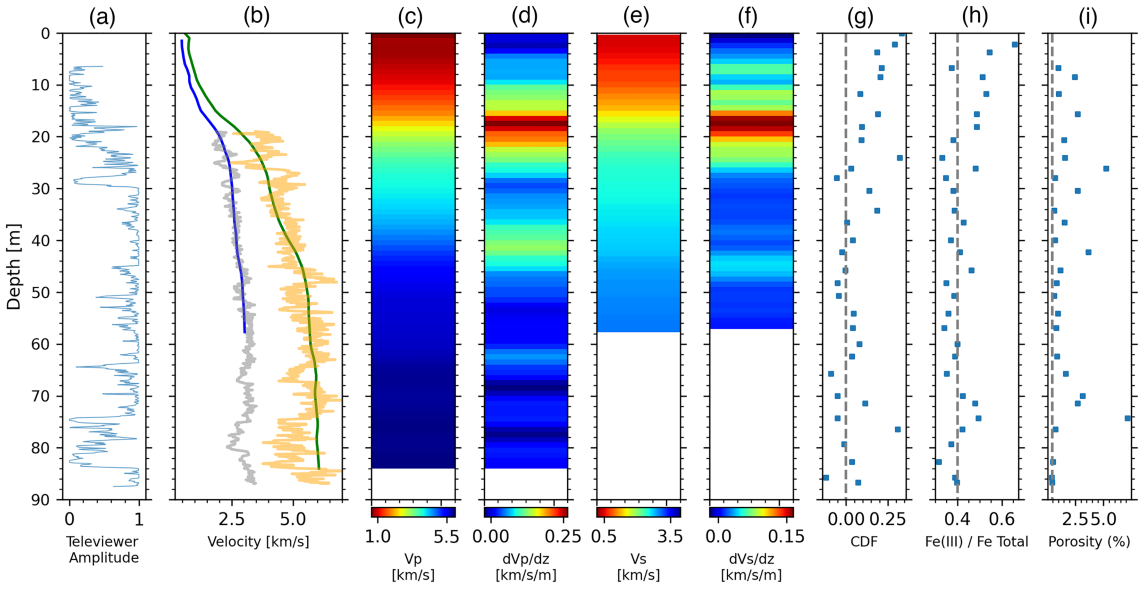


**FIGURE 9** Summary of the information at the borehole location: (a) normalized televiewer amplitude data; (b) seismic velocity data from P-wave velocity from body wave tomography (green), S-wave velocity from MASW (blue), P-wave velocity from sonic log (yellow), and S-wave velocity from sonic log (grey); (c) colour plot of P-wave velocity; (d) colour plot of P-wave vertical velocity gradient; (e) colour plot of S-wave velocity; (f) colour plot of S-wave vertical velocity gradient; (g, h) Fe(III)/Fe total and porosity data. Dashed lines in (g), (h), and (i) shows the mean value [Color figure can be viewed at wileyonlinelibrary.com]

the MASW and body wave tomography methods, we managed to model the seismic velocity structure at the shallow part of the subsurface between 0 and 20 m depth. At the borehole location, both P-wave velocities from the body wave tomography and S-wave velocities from the MASW model are in good agreement with the sonic log-derived velocities (Figure 9b). However, as expected, both the MASW and body wave tomography methods could not resolve the fine scale revealed by the sonic log as the methods present different frequency content. Sonic logs use a higher seismic wave frequency, and thus are able to resolve the fine details, while the body and surface wave methods represent lower frequency content and are limited by the wavelength resolution.

In Figures 9c and e, we also present the P- and S-wave velocity as coloured images. We use the same colour scale for both images, with the P-wave colour scale adjusted as 1.8 times the S-wave colour scale. Comparing Figures 9c and e, we can see that we have a consistent feature of a low absolute P- and S-wave velocity value in the upper 16 m (blue to light green colour). Below 16 m depth, P- and S-wave velocity values increase steeply as shown by the vertical velocity gradient images in panels D and F. The relatively high vertical velocity gradient (indicated by red colours) shows a clear transition between the upper layer with relatively low P- and S-wave velocity and the relatively higher P- and S-wave velocity layer below.

## 5.2 | Seismic expression of the weathering structure

We identified three major layers from the seismic results. When calibrated by the borehole data, the layers are: saprolite, weathered bedrock, and bedrock. As shown in Figure 9, each layer has different characteristics, especially in terms of seismic velocity. By combining our geophysical results with the geochemical data from Krone et al. (2021), we discuss the possible layer interpretation as summarized in Figure 10. The interpreted saprolite and weathered bedrock layers reach 30 m depth, which we interpret as the extent of the weathering front. We use the layers identified at the borehole to produce a 2D interpretation of the seismic profile.

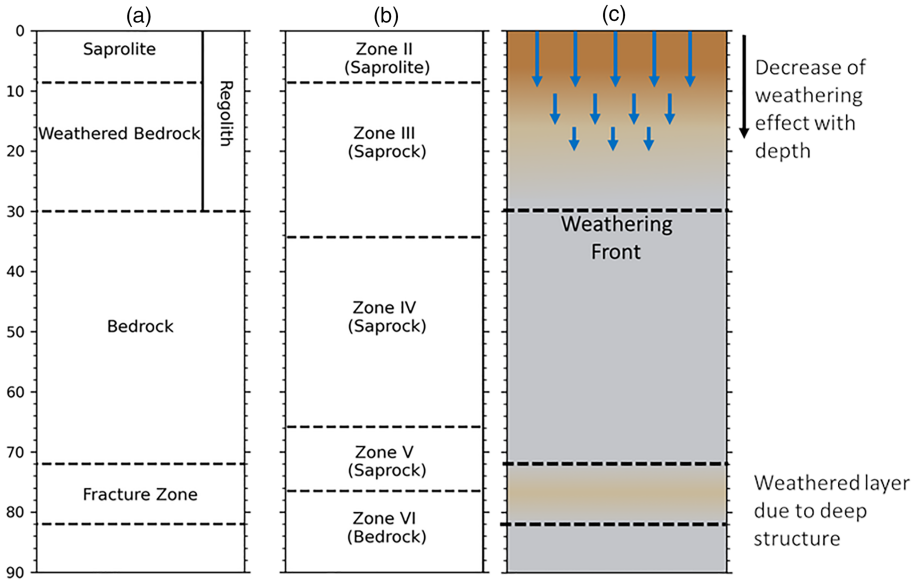


**FIGURE 10** Critical zone structure in the Santa Gracia reserve: (a) from seismic and borehole data; (b) from geochemical data; (c) conceptual process model. From top to bottom, we identified saprolite and weathered bedrock which forms the regolith down to 30 m depth [Color figure can be viewed at wileyonlinelibrary.com]

## 5.3 | Saprolite

In a previous study on a similar granitic environment in Wyoming, Flinchum et al. (2018) suggested using the depth of the borehole casing as an indirect indication of the boundary between saprolite and weathered bedrock. Following this approach, the borehole casing depth in the study site is located at 6 m depth and attributed to P- and S-wave velocity of 0.8 and 0.6 km/s, respectively. These P- and S-wave velocity values are considerably lower than the P-wave velocity of 1.2 km/s suggested by Flinchum et al. (2018). Inversely, when we consider the P-wave velocity value of 1.2 km/s as the marker for the bottom of the saprolite layer, we reach a depth of 10 m. On the other hand, based on geochemical interpretation of samples taken from the borehole core, Krone et al. (2021) identified the depth range of 0.1–8.6 m as the saprolite layer, followed by a saprock layer as shown in Figure 10b. Based on this interpretation, the bottom of the saprolite layer in the borehole would correspond to a P-wave velocity of 1.05 km/s and an S-wave velocity of 0.75 km/s.

We attribute the difference in the identified seismic velocity of the saprolite layer between our work and the study by Flinchum et al. (2018) to the different protolith encountered in Santa Gracia and the Blair–Wallis critical zone (BWCZ) in Wyoming. In addition, the degree of weathering is also likely to account for different seismic velocities of the saprolite in both field sites. For example, the observed saprolite S-wave velocity in Santa Gracia shows a value of 0.75 km/s at 8.6 m depth and is relatively higher compared to the S-wave velocity of 0.6 km/s used to identify the saprolite layer in the BWCZ (Keifer et al., 2019). The higher S-wave velocity found in our data is likely to be attributed to the different weathering degrees of the saprolite. Nevertheless, we consider the difference to be reasonable and the layering visible in the P- and S-wave velocity images further strengthens the interpretation of saprolite occurring down to 8.6 m depth (Krone et al., 2021).

Another characteristic in the upper 8.6 m is the relatively constant P- and S-wave velocity as also shown by the low vertical velocity gradient (Figures 8c–f). This could indicate a relatively homogenous saprolite layer in terms of physical properties and composition. We expect that down to 8.6 m depth, the layer is highly affected by surface-related weathering processes. However, since the velocity gradient around the 8.6 m depth is also relatively low, we consider the interface between the saprolite and the underlying weathered bedrock to be more transitional and not of a sharp boundary. The transition can be attributed to a decreasing weathering rate with depth (Brantley et al., 2008).

## 5.4 | Weathered bedrock

We identified weathered bedrock from the bottom of the saprolite at 8.6 m to a depth of 30 m in the borehole location. The bottom of the weathered bedrock layer was identified based on a P-wave velocity of 4.0 km/s (Flinchum et al., 2018), which will be discussed in detail in the bedrock discussion. While Krone et al. (2021) interpreted the layer between 8.6 and 34.3 m depth as a single unit, the televiewer, sonic log, as well as the P- and S-wave velocity data (Figure 9) indicate another significant change of lithology around 16 m depth. At this depth range, we observe a P-wave velocity of 2.0 km/s and an S-wave velocity of 1.36 km/s. Previous P-wave velocity studies on a weathered granite environment in Spain chose this 2.0 km/s P-wave velocity to mark the boundary between saprolite and moderately weathered bedrock (Begonha & Sequeira Braga, 2002; Olona et al., 2010). The relatively high vertical velocity gradient of the P- and S-wave in our data also coincides with this 2.0 km/s marker, which indicates greater heterogeneity than indicated in the single zone identified by Krone et al. (2021). The high vertical velocity gradient of the P- and S-wave could indicate a sharper lithology change, especially at the peak between 16 and 20 m depth. Based on this observation, we expect that the layer between 8.6 and 16 m depth underwent stronger weathering compared to the layer between 16 and 34.3 m depth.

Intuitively, we tried to attribute the sudden increase in P- and S-wave velocity shown by the high vertical velocity gradient between 16 and 20 m depth to closures of pores and fractures with increasing depth. However, the porosity data in Figure 9i does not show significant changes of porosity over this depth range. On the other hand, the Fe (III)/Fe total information provided in Krone et al. (2021) shows a relatively high iron reduction in the upper 16 m (Figure 9h). The differing features between the porosity and iron redox information could indicate that the weathering processes down to 16 m depth can be

attributed more to iron reduction by dissolution processes than to increase of porosity. Additionally, reactions of Fe minerals can increase strain in the rock and trigger weathering-induced micro-fracturing (Behrens et al., 2015; Fletcher et al., 2006). It is, however, difficult to prove this relation without fracture density data from the core.

For a depth range of 16–34.3 m, we expect different weathering processes compared to the weathering process in the upper layer (<16 m depth). Based on the observation of high chemical depletion factor (CDF; Figure 9g), we relate the weathering of the bedrock layer down to 16 m depth to chemical alteration due to water infiltrating from precipitation at the surface. In contrast, the low iron reduction and sharp increase in seismic velocities of the weathered bedrock from 16 to 30 m depth suggest weathering that is unrelated to surface-derived fluids. Instead, we expect the sharp increase of seismic velocities to be due to the change of physical properties.

## 5.5 | Bedrock

The P-wave velocity data in Figure 9b show that velocities >4.0 km/s occur at 30 m depth. Previous studies in BWCZ suggest that the 4.0 km/s P-wave velocity can be used as a marker to identify the top of granite bedrock (Callahan et al., 2020; Flinchum et al., 2018). Therefore, we identify the top of the bedrock at ~30 m depth. This interpretation is also supported by the observation of the high televiewer amplitude below 30 m depth (Figure 9a).

The 4.0 km/s velocity marker at 30 m depth also occurs below a relatively steep vertical velocity gradient, similar to what has been observed in the BWCZ (Flinchum et al., 2018). At the same depth, and also beneath a relatively steep S-wave velocity gradient, the S-wave velocity shows a value of 2.5 km/s (Figures 9d and e). High P-wave velocities extend down to 80 m and reach up to 5.0 km/s at ~40 m. The acoustic televiewer in Figure 9a also shows rather constant amplitudes down to 75 m. We interpreted the layer with a decrease of acoustic televiewer amplitudes and lowered sonic P- and S-wave velocities between 72 and 82 m depth as a local zone of mechanical weakness such as a fault zone. However, we lack the necessary information for further interpretation of these features.

With the interpreted top of the bedrock at 30 m depth, we identify the weathering front at our borehole location to reach down to 30 m depth, which includes the saprolite and weathered bedrock layer as the regolith, as shown in Figure 10a. Based on geochemical data, Krone et al. (2021) argue for multiple weathering fronts, with the first one located at ~35 m depth. While the geochemical interpretation provided a different interpretation, the depth difference is not significant (<5 m) and the P- and S-wave velocity still manages to provide a relatively good match with the interpreted layer by Krone et al. (2021), especially for the saprolite and weathered bedrock layer. The differing interpretation can be attributed to how the geochemical interpretation attributes the existence of chemical reactions such as oxidation as evidence of weathering processes. However, the physical characteristics of the bedrock with a P-wave velocity >4.0 km/s is attributed more to the crystalline fresh bedrock, and chemical weathering in this lithology would be limited to fracture surfaces (Flinchum et al., 2018).

The hypothesized major decrease in surface-related weathering effect from 16 m depth (Figure 10c) requires further evidence. This hypothesis is mainly driven by the iron reduction data shown in Figure 9h and the high vertical velocity gradient shown in Figures 9d and f. Nevertheless, the extent of the weathered bedrock from our data at 30 m depth generally agrees with the interpreted Zone III from the geochemical data interpretation at 34.6 m depth. As for the bottom of the saprolite layer, we find a good agreement between the geophysical data and geochemical data.

## 5.6 | Lateral extent

The interpretation of the weathering structure as calibrated at the borehole is finally applied along the entire seismic profile (Figure 11a). While the weathering front is identified around the 30 m depth at the borehole location, laterally the weathering front shows variations relative to the topography. This variation is most pronounced for the relatively thick saprolite and weathered bedrock layer 300–400 m profile distance, as shown also in Figure 11b. While we can intuitively relate the thickening of the regolith to alluvial accumulation in the valley bottom, that is not the case in our seismic profile as an alluviated valley will show a stronger relief—as shown in the northwestern part of the seismic profile (Figure 2b). Therefore, we expect that any varying weathering front depth across the profile is due to the different effect of weathering processes.

The low televiewer amplitude between 72 and 82 m depth (Figure 9a), as also observed in the geochemical analysis by Krone et al. (2021), coincides with a slight velocity distortion shown in the conceptual model (Figure 11a). We therefore speculate that the zone of low televiewer amplitude could be related to a larger geological structure, such as a fault. Such a structure could provide the pathway for surface-derived water to infiltrate into the deeper subsurface and enable chemical weathering at depth (Holbrook et al., 2019). However, further evidence is needed to support the hypothesis that the identified feature is part of a larger structure. For example, should geochemical analyses show indications of meteoric water in the fracture zone, the structure may be linked to the surface.

To estimate the regolith residence time, we can divide the regolith thickness (~27 m) by an estimate of the denudation rate of ~11 m/Myr, based on cosmogenic nuclides (Krone et al., 2021). This results in a turnover time of the regolith of ~2.5 Myr, which covers the whole Quaternary period. Such a long time period suggests that the processes involved in creating the weathering zone we observe in Santa Gracia must be operating over geological time scales. Short-term variations that may occur over orbital or glacial–interglacial time scales are therefore less likely to affect the thickness of the weathering zone significantly.

## 5.7 | Controlling processes

The identified structure of the critical zone in Santa Gracia is a result of various controlling processes which affect the surface and subsurface characteristics and structures of the critical zone. To understand these processes, we compare our conceptual model in Figure 11a to various geomorphological models of the critical zone that make explicit predictions about the depth of the weathering zone.

Traditional models of weathering advance suggest a 'top-down' control due to the infiltration of meteoric water into the bedrock,

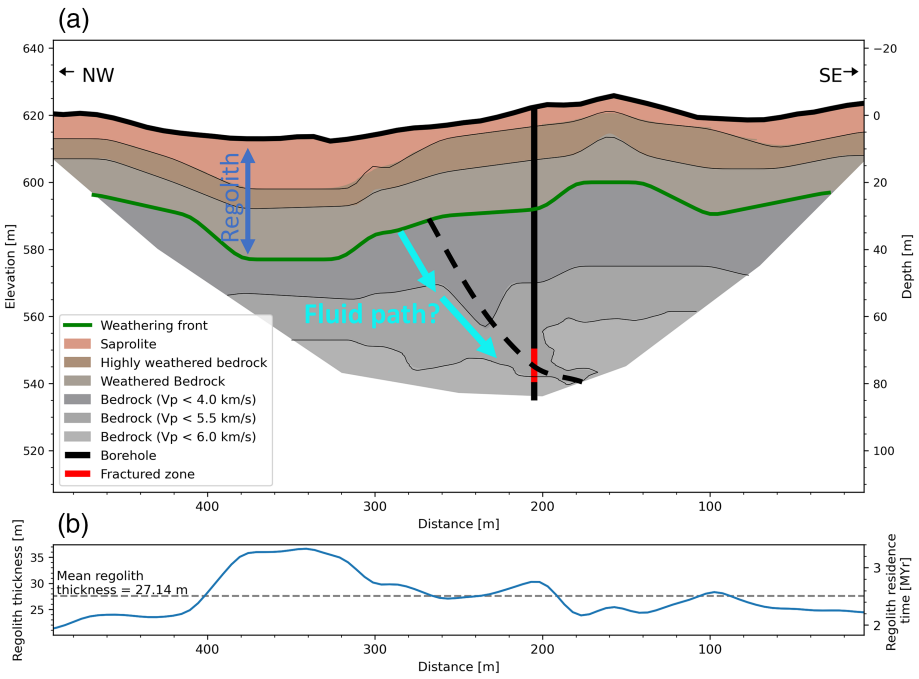


**FIGURE 11** (a) Conceptual model of the measured seismic profile from combined P- and S-wave velocity information. Black line shows the borehole location, with the red line indicating the relatively weak zone detected in the televiewer data. The conceptual model is shown with vertical exaggeration (VE) of 2:1. (b) Estimated regolith thickness across the profile with observed thinning around topographic high (~150 m distance) and thickening around topographic low (300–400 m distance) [Color figure can be viewed at wileyonlinelibrary.com]

which drives chemical reactions in the subsurface (Brantley & White, 2009). The downward infiltration of meteoric water will continue as permeability allows and induce weathering processes until the water reaches chemical equilibrium. Following this hypothesis and assuming a homogenous bedrock across our profile, we expect a weathering depth that is parallel to the surface topography. However, the saprolite in our model appears to be thinner in the topographic high, especially around the 120–360 m profile distance. Inversely, we observed thicker saprolite at topographic lows. Based on this observation, and following the 'top-down' hypothesis, we may conclude that the different weathering depths are due to different bedrock characteristics along the profile. For example, bedrock with higher fracture density at the topographic low would allow for deeper penetrating weathering (Brantley et al., 2017; Lodes et al., 2021). With the current data set, however, we are unable to provide clear evidence of different fracture density along the profile. Further seismic analysis which considers seismic anisotropy and bedrock fracture density data could help in testing this hypothesis in future works.

In contrast to the 'top-down' control, Rempe and Dietrich (2014) proposed a 'bottom-up' control, in which the thickness of the weathered zone is controlled by whether the bedrock can be drained. This drainage is largely determined by the topographic profile on the surface and the groundwater profile in the subsurface. The hypothesis predicts a thickening of the weathered zone in topographic highs (upslope) and a thinning of the weathered zone towards channels (here, the topographic lows). This prediction is opposite to what we observe in Santa Gracia National Reserve. The difference compared to the model presented by Rempe and Dietrich (2014) could be related to the aridity and the absence of perennial flow in our study area.

Another model of regolith formation was presented by Braun et al. (2016), who hypothesized that the depth of the weathering front is limited by the ability of groundwater to transfer solutes before the reacting fluids reach saturation. The model predicts steady-state regolith thickness as a function of topography (length and slope), uplift rate, erosion rate, weathering rate, hydraulic conductivity, and surface transport coefficient. In an arid landscape, the model predicts a thicker regolith at the top of a hill, similar to the bottom-up model of Rempe and Dietrich (2014). On the other hand, where the precipitation rate is high and/or the uplift rate is low, the model predicts a thicker regolith under topographic lows. In Santa Gracia, which is located in an arid area (Karger et al., 2017; Werner et al., 2018), we observe that regolith is relatively thicker in the topographic low. Braun et al. (2016) have also shown, however, that changes in precipitation can have striking results on spatial variations in regolith thickness. In Santa Gracia, where the estimated time scale of regolith formation covers the entire Quaternary period, the present-day thickness of the regolith could thus be the result of very different climates in the recent geological past. In addition, Braun et al. (2016) have shown that in eroding landscapes, changes in precipitation can have striking results on spatial variations in regolith thickness. In Santa Gracia, where the estimated time scale of regolith formation covers the entire Quaternary period, the present-day thickness of the regolith could thus be the result of very different climates in the recent geological past.

In a transient experiment by Braun et al. (2016), in which the critical zone transitions from saturated to unsaturated conditions, the downslope trend in regolith thickness switches trend and eventually attains a relatively uniform thickness. Specifically, when precipitation and uplift rates are low and the regolith is unsaturated, their model predicts a regolith layer that is thinning towards the topographic high. Based on this comparison, it is likely that the critical zone structure in our study site is in a transient state and going through a continuous process of desaturation of the regolith, which could be linked to the aridification of the Atacama Desert.

In addition to the existing regolith thickness prediction models, which consider the groundwater level, we also investigate a geomorphological model which predicts possible fractured bedrock. We first compare our conceptual model with the topographic stress model presented by Slim et al. (2014). The model used a two-dimensional boundary element method to calculate the minimum cohesion

required to prevent shear failure as a proxy for potential fracturing. The study shows that in valleys/topographic lows, the bedrock is more likely to have shear fractures compared to bedrock at hills/topographic highs. When we consider the thicker regolith in the topographic low at our study site, we can also assume that this behaviour is due to the higher fracture density in the valley of our model. With higher fracture density, the bedrock in this valley will be easier to weather and thus to develop a deeper regolith. The study also shows rapid decline of $C_{min}$ in the upper 15 m, which we speculate can be related to a rapid increase of seismic velocity as shown in Figure 9b. However, a more detailed analysis of the rock's physics, especially in the borehole location, is still needed to investigate this hypothesis.

Further modelling of the effect of topographic stress on bedrock was also presented by St. Clair et al. (2015). In the presented failure potential model, abundance of fracture in the bedrock is controlled by the ratio between tectonic stress and gravitational stress ($\sigma^*$). The model predicts that in areas with low tectonic compression or widely spaced ridges and valleys, the depth of the weathered rock will be relatively uniform in space. Considering that the Chilean coastal cordillera is a tectonically active area, where tectonic stresses are large (>7 MPa around 36°S; Luttrell et al., 2011), we estimate $\sigma^* > 0.75$. With $\sigma^* < 1.0$, the model predicts that the weathered rocks across the landscape will be parallel to the surface topography, which does not match completely with our observation. One possible explanation for this difference is that the observed model that we present is already a result of complex interaction between different weathering processes, which is not completely considered by the topographic stress modelling.

## 6 | CONCLUSION AND OUTLOOK

In this study, we seismically imaged the weathering structure in the Santa Gracia Reserve in Chile using body wave tomography and the MASW method. The resulting P- and S-wave velocity models agree with available borehole information and, moreover, complement the missing upper 20 m of the sonic log data and support the existing geochemical interpretation. Across the surveyed seismic profile, we estimate a mean weathering front depth of ca. 27 m and identified saprolite thickness variations at minor topographic highs and lows. The vertical velocity gradients of the P- and S-wave velocities provide a complementary perspective on the lithological character at depth and evidence additional subtle features within the different layers. For example, a high-velocity gradient can be related to the rapid changes in the rock's physical properties or mineral composition. The identified weak zone at depth in the borehole data can be related to a possible fault, however, further investigation of such features is still required, with both geophysical and geochemical approaches.

The seismic, borehole, and geochemical results allow us to derive an integrated interpretation of the weathering structure. While we found some differences between the geophysical and geochemical interpretation, both data sets complement and strengthen one another. Therefore, we suggest that geophysical investigation using the seismic method with both body and surface waves will enhance other near-surface investigations of the critical zone.

Comparison to different models of regolith evolution shows that the conceptual model we have in Santa Gracia cannot be attributed to any single specific model. While the study area has only limited precipitation and no water table, it is likely that the effect of the limited precipitation still affects the advance of regolith due to water infiltration. It is important to note that regolith formation covers the entire Quaternary period and thus integrates over different climate conditions during this time period. On the other hand, the infiltration of water into the subsurface requires a certain level of permeability, which can be related to the opening of fractures in the bedrock as a result of topographic and tectonic stresses. Therefore, the development of a regolith evolution model, which couples both aspects, can be important for future studies of the weathering zone.

## ACKNOWLEDGEMENTS

We acknowledge support from the German Science Foundation (DFG) priority research programme SPP-1803 'EarthShape: Earth Surface Shaping by Biota' (Grant No. KR 2073/5-1 to Charlotte M. Krawczyk). We thank CONAF and Park Rangers for the possibility of working in the national parks, as well as providing access to the research site. We thank Martin Krüger and our colleagues at the University of Concepción for their assistance during seismic data acquisition in Santa Gracia, Chile. We also thank Geophysical Instrument Pool Potsdam (GIPP) for providing all the necessary equipment for the seismic campaign. The reviews from two anonymous reviewers greatly helped to improve the manuscript. Open Access funding enabled and organized by Projekt DEAL.

## DATA AVAILABILITY STATEMENT

The data that support the findings will be available in the GFZ Data Repository following an embargo to allow for doctoral publication of research findings.

## ORCID

*Rahmantara Trichandi* https://orcid.org/0000-0002-4536-9202
*Klaus Bauer* https://orcid.org/0000-0002-7777-2653
*Trond Ryberg* https://orcid.org/0000-0001-7129-5596
*Dirk Scherler* https://orcid.org/0000-0003-3911-2803
*Klaus Bataille* https://orcid.org/0000-0001-6006-6747
*Charlotte M. Krawczyk* https://orcid.org/0000-0002-5505-6293

## REFERENCES

Bauer, K., Moeck, I., Norden, B., Schulze, A., Weber, M. & Wirth, H. (2010) Tomographic *P* wave velocity and vertical velocity gradient structure across the geothermal site Groß Schönebeck (NE German Basin): Relationship to lithology, salt tectonics, and thermal regime. *Journal of Geophysical Research*, 115(B8), B08312. Available from: https://doi.org/10.1029/2009jb006895

Baumann-Wilke, M., Bauer, K., Schovsbo, N.H. & Stiller, M. (2012) P-wave traveltime tomography for a seismic characterization of black shales at shallow depth on Bornholm, Denmark. *Geophysics*, 77(5), EN53–EN60. Available from: https://doi.org/10.1190/geo2011-0326.1

Bazilevskaya, E., Lebedeva, M., Pavich, M., Rother, G., Parkinson, D.Y., Cole, D. et al. (2013) Where fast weathering creates thin regolith and slow weathering creates thick regolith. *Earth Surface Processes and Landforms*, 38(8), 847–858. Available from: https://doi.org/10.1002/esp.3369

Befus, K.M.M., Sheehan, A.F.F., Leopold, M., Anderson, S.P.P. & Anderson, R.S.S. (2011) Seismic constraints on critical zone architecture, Boulder Creek watershed, front range, Colorado. *Vadose Zone Journal*, 10(3), 915–927. Available from: https://doi.org/10.2136/vzj2010.0108

Begonha, A. & Sequeira Braga, M. (2002) Weathering of the Oporto granite: Geotechnical and physical properties. *Catena*, 49(1–2), 57–76. Available from: https://doi.org/10.1016/S0341-8162(02)00016-4

Behrens, R., Bouchez, J., Schuessler, J.A., Dultz, S., Hewawasam, T. & Von Blanckenburg, F. (2015) Mineralogical transformations set slow weathering rates in low-porosity metamorphic bedrock on mountain slopes in a tropical climate. *Chemical Geology*, 411, 283–298. Available from: https://doi.org/10.1016/j.chemgeo.2015.07.008

Bernhard, N., Moskwa, L.M., Schmidt, K., Oeser, R.A., Aburto, F., Bader, M. Y. et al. (2018) Pedogenic and microbial interrelations to regional climate and local topography: New insights from a climate gradient (arid to humid) along the coastal cordillera of Chile. *Catena*, 170, 335–355. Available from: https://doi.org/10.1016/j.catena.2018.06.018

Bodin, T. (2010) *Transdimensional approaches to geophysical inverse problems*. PhD thesis, Claude Bernard University Lyon 1. https://doi.org/10.1021/jo00151a027

Brantley, S.L., Bandstra, J., Moore, J. & White, A.F. (2008) Modelling chemical depletion profiles in regolith. *Geoderma*, 145(3–4), 494–504. Available from: https://doi.org/10.1016/j.geoderma.2008.02.010

Brantley, S.L., Goldhaber, M.B. & Vala Ragnarsdottir, K. (2007) Crossing disciplines and scales to understand the critical zone. *Elements*, 3(5), 307–314. Available from: https://doi.org/10.2113/gselements.3.5.307

Brantley, S.L., Lebedeva, M.I., Balashov, V.N., Singha, K., Sullivan, P.L. & Stinchcomb, G. (2017) Toward a conceptual model relating chemical reaction fronts to water flow paths in hills. *Geomorphology*, 277, 100–117. Available from: https://doi.org/10.1016/j.geomorph.2016.09.027

Brantley, S.L. & White, A.F. (2009) Approaches to modeling weathered regolith. In: Oelkers, E.H. & Schott, J. (Eds.) *Thermodynamics and Kinetics of Water–Rock Interaction*. Berlin: De Gruyter, pp. 435–484 https://doi.org/10.1515/9781501508462-012

Brantut, N. & David, E.C. (2019) Influence of fluids on $V_P/V_S$ ratio: Increase or decrease? *Geophysical Journal International*, 216(3), 2037–2043. Available from: https://doi.org/10.1093/gji/ggy518

Braun, J., Mercier, J., Guillocheau, F. & Robin, C. (2016) A simple model for regolith formation by chemical weathering. *Journal of Geophysical Research – Earth Surface*, 121(11), 2140–2171. Available from: https://doi.org/10.1002/2016JF003914

Callahan, R.P., Riebe, C.S., Pasquet, S., Ferrier, K.L., Grana, D., Sklar, L.S. et al. (2020) Subsurface weathering revealed in hillslope-integrated porosity distributions. *Geophysical Research Letters*, 47(15), e2020GL088322. Available from: https://doi.org/10.1029/2020gl088322

Comina, C., Krawczyk, C.M., Polom, U. & Socco, L.V. (2017) Integration of SH seismic reflection and love-wave dispersion data for shear wave velocity determination over quick clays. *Geophysical Journal International*, 210(3), 1922–1931. Available from: https://doi.org/10.1093/gji/ggx276

Dal Bo, I., Klotzsche, A., Schaller, M., Ehlers, T.A., Kaufmann, M.S., Fuentes Espoz, J.P. et al. (2019) Geophysical imaging of regolith in landscapes along a climate and vegetation gradient in the Chilean coastal cordillera. *Catena*, 180, 146–159. Available from: https://doi.org/10.1016/j.catena.2019.04.023

Fletcher, R.C., Buss, H.L. & Brantley, S.L. (2006) A spheroidal weathering model coupling porewater chemistry to soil thicknesses during steady-state denudation. *Earth and Planetary Science Letters*, 244 (1–2), 444–457. Available from: https://doi.org/10.1016/j.epsl.2006.01.055

Flinchum, B.A., Holbrook, W.S., Rempe, D., Moon, S., Riebe, C.S., Carr, B.J. et al. (2018) Critical zone structure under a granite ridge inferred from drilling and three-dimensional seismic refraction data. *Journal of Geophysical Research – Earth Surface*, 123(6), 1317–1343. Available from: https://doi.org/10.1029/2017JF004280

Gobierno de Chile Servicio Nacional de Geologia y Mineria. (2003) *Mapa Geologico de Chile: Version Digital*.

Graham, R.C., Rossi, A.M. & Hubbert, K.R. (2010) Rock to regolith conversion: Producing hospitable substrates for terrestrial ecosystems. *GSA Today*, 20(2), 4–9. Available from: https://doi.org/10.1130/GSAT57A.1

Hayes, N.R., Buss, H.L., Moore, O.W., Krám, P. & Pancost, R.D. (2020) Controls on granitic weathering fronts in contrasting climates. *Chemical Geology*, 535(March 2019), 119450. Available from: https://doi.org/10.1016/j.chemgeo.2019.119450

Holbrook, W.S., Marcon, V., Bacon, A.R., Brantley, S.L., Carr, B.J., Flinchum, B.A. et al. (2019) Links between physical and chemical weathering inferred from a 65-m-deep borehole through Earth's critical zone. *Scientific Reports*, 9(1), 4495–5005. Available from: https://doi.org/10.1038/s41598-019-40819-9

Holbrook, W.S., Riebe, C.S., Elwaseif, M., Hayes, J.L., Basler-Reeder, K., Harry, D.L. et al. (2014) Geophysical constraints on deep weathering and water storage potential in the Southern Sierra critical zone observatory. *Earth Surface Processes and Landforms*, 39(3), 366–380. Available from: https://doi.org/10.1002/esp.3502

Ivanov, J., Miller, R.D., Lacombe, P., Johnson, C.D. & Lane, J.W. (2006) Delineating a shallow fault zone and dipping bed rock strata using multichannel analysis of surface waves with a land streamer. *Geophysics*, 71(5), A39–A42. Available from: https://doi.org/10.1190/1.2227521

Karger, D.N., Conrad, O., Böhner, J., Kawohl, T., Kreft, H., Soria-Auza, R.W. et al. (2017) Climatologies at high resolution for the earth's land surface areas. *Scientific Data*, 4, 1–20. Available from: https://doi.org/10.1038/sdata.2017.122

Keifer, I., Dueker, K. & Chen, P. (2019) Ambient Rayleigh wave field imaging of the critical zone in a weathered granite terrain. *Earth and Planetary Science Letters*, 510, 198–208. Available from: https://doi.org/10.1016/j.epsl.2019.01.015

Konstantaki, L.A., Ghose, R., Draganov, D., Diaferia, G. & Heimovaara, T. (2015) Characterization of a heterogeneous landfill using seismic and electrical resistivity data. *Geophysics*, 80(1), EN13–EN25. Available from: https://doi.org/10.1190/geo2014-0263.1

Krone, L.V., Hampl, F.J., Schwerdhelm, C., Bryce, C., Ganzert, L., Kitte, A. et al. (2021) Deep weathering in the semi-arid coastal cordillera, Chile. *Scientific Reports*, 11(1), 1–15. Available from: https://doi.org/10.1038/s41598-021-90267-7

Kukowski, N. & Oncken, O. (2006) Subduction erosion – the "normal" mode of fore-arc material transfer along the Chilean margin? In: Oncken, O., & Kukowski, N. (Eds.) *The Andes*. Berlin: Springer, pp. 217–236 https://doi.org/10.1007/978-3-540-48684-8_10

Leone, J.D., Holbrook, W.S., Riebe, C.S., Chorover, J., Ferré, T.P.A., Carr, B. J. et al. (2020) Strong slope-aspect control of regolith thickness by bedrock foliation. *Earth Surface Processes and Landforms*, 45(12), 2998–3010. Available from: https://doi.org/10.1002/esp.4947

Lodes, E., Scherler, D., Wittmann, H. & van Dongen, R. (2021) Patchy bedrock explained: Tectonic fracture control on landscape evolution patterns in South-Central Chile. *EGU General Assembly*, 19–30 April, EGU2021--9231.

Luttrell, K.M., Tong, X., Sandwell, D.T., Brooks, B.A. & Bevis, M.G. (2011) Estimates of stress drop and crustal tectonic stress from the 27 February 2010 Maule, Chile, earthquake: Implications for fault strength. *Journal of Geophysical Research: Solid Earth*, 116(B11), B11401. Available from: https://doi.org/10.1029/2011jb008509

Miller, R.D., Xia, J., Park, C.B. & Ivanov, J.M. (1999) Multichannel analysis of surface waves to map bedrock. *The Leading Edge*, 18(12), 1392–1396. Available from: https://doi.org/10.1190/1.1438226

Oeser, R.A., Stroncik, N., Moskwa, L.M., Bernhard, N., Schaller, M., Canessa, R. et al. (2018) Chemistry and microbiology of the critical zone along a steep climate and vegetation gradient in the Chilean coastal cordillera. *Catena*, 170, 183–203. Available from: https://doi.org/10.1016/j.catena.2018.06.002

Oeser, R.A. & Von Blanckenburg, F. (2020) Do degree and rate of silicate weathering depend on plant productivity? *Biogeosciences*, 17(19), 4883–4917. Available from: https://doi.org/10.5194/bg-17-4883-2020

Olona, J., Pulgar, J.A., Fernández-Viejo, G., López-Fernández, C. & González-Cortina, J.M. (2010) Weathering variations in a granitic massif and related geotechnical properties through seismic and

electrical resistivity methods. *Near Surface Geophysics*, 8(6), 585–599. Available from: https://doi.org/10.3997/1873-0604.2010043

Park, C.B., Miller, R.D., Ryden, N., Xia, J. & Ivanov, J. (2005) Combined use of active and passive surface waves. *Journal of Environmental and Engineering Geophysics*, 10(3), 323–334. Available from: https://doi.org/10.2113/JEEG10.3.323

Park, C.B., Miller, R.D. & Xia, J. (1999) Multichannel analysis of surface waves. *Geophysics*, 64(3), 800–808. Available from: https://doi.org/10.1190/1.1444590

Pasquet, S. & Bodet, L. (2017) SWIP: An integrated workflow for surface-wave dispersion inversion and profiling. *Geophysics*, 82(6), WB47–WB61. Available from: https://doi.org/10.1190/GEO2016-0625.1

Pasquet, S., Bodet, L., Dhemaied, A., Mouhri, A., Vitale, Q., Rejiba, F. et al. (2015) Detecting different water table levels in a shallow aquifer with combined P-, surface and SH-wave surveys: Insights from $V_P/V_S$ or Poisson's ratios. *Journal of Applied Geophysics*, 113, 38–50. Available from: https://doi.org/10.1016/j.jappgeo.2014.12.005

Rempe, D.M. & Dietrich, W.E. (2014) A bottom-up control on fresh-bedrock topography under landscapes. *Proceedings of the National Academy of Sciences of the United States of America*, 111(18), 6576–6581. Available from: https://doi.org/10.1073/pnas.1404763111

Ryberg, T. & Haberland, C. (2019) Bayesian simultaneous inversion for local earthquake hypocentres and 1-D velocity structure using minimum prior knowledge. *Geophysical Journal International*, 218(2), 840–854. Available from: https://doi.org/10.1093/gji/ggz177

Slim, M., Perron, J.T., Martel, S.J. & Singha, K. (2014) Topographic stress and rock fracture: a two-dimensional numerical model for arbitrary topography and preliminary comparison with borehole observations. *Earth Surface Processes and Landforms*, 40(4), 512–529. Available from: https://doi.org/10.1002/esp.3646

St. Clair, J., Moon, S., Holbrook, W.S., Perron, J.T., Riebe, C.S., Martel, S.J. et al. (2015) Geophysical imaging reveals topographic stress control of bedrock weathering. *Science*, 350(6260), 534–538. Available from: https://doi.org/10.1126/science.aab2210

Stierman, D.J. & Healy, J.H. (1984) A study of the depth of weathering and its relationship to the mechanical properties of near-surface rocks in the Mojave Desert. *Pure and Applied Geophysics*, 122(2–4), 425–439. Available from: https://doi.org/10.1007/BF00874609

Thurber, C. & Eberhart-Phillips, D. (1999) Local earthquake tomography with flexible gridding. *Computers and Geosciences*, 25(7), 809–818. Available from: https://doi.org/10.1016/S0098-3004(99)00007-2

Vázquez, M., Ramírez, S., Morata, D., Reich, M., Braun, J.J. & Carretier, S. (2016) Regolith production and chemical weathering of granitic rocks in Central Chile. *Chemical Geology*, 446, 87–98. Available from: https://doi.org/10.1016/j.chemgeo.2016.09.023

Wadas, S.H., Tschache, S., Polom, U. & Krawczyk, C.M. (2020) Ground instability of sinkhole areas indicated by elastic moduli and seismic attributes. *Geophysical Journal International*, 222(1), 289–304. Available from: https://doi.org/10.1093/gji/ggaa167

Wang, W., Chen, P., Keifer, I., Dueker, K., Lee, E.J., Mu, D. et al. (2019) Weathering front under a granite ridge revealed through full-3D seismic ambient-noise tomography. *Earth and Planetary Science Letters*, 509, 66–77. Available from: https://doi.org/10.1016/j.epsl.2018.12.038

Wathelet, M., Chatelain, J.L., Cornou, C., Di Giulio, G., Guillier, B., Ohrnberger, M. et al. (2020) Geopsy: A user-friendly open-source tool set for ambient vibration processing. *Seismological Research Letters*, 91(3), 1878–1889. Available from: https://doi.org/10.1785/0220190360

Weckmann, U., Bauer, K., Krawczyk, C., Kück, J., Übernickel, K. & von Blanckenburg, F. (2020) *Geophysical Borehole Logging Data from Santa Gracia*. Chile: GFZ Data Services. https://doi.org/10.5880/GFZ.2.7.2020.001

Werner, C., Schmid, M., Ehlers, T.A., Fuentes-Espoz, J.P., Steinkamp, J., Forrest, M. et al. (2018) Effect of changing vegetation and precipitation on denudation – Part 1: Predicted vegetation composition and cover over the last 21 thousand years along the coastal cordillera of Chile. *Earth Surface Dynamics*, 6(4), 829–858. Available from: https://doi.org/10.5194/esurf-6-829-2018

Yaede, J.R., McBride, J.H., Nelson, S.T., Park, C.B., Flores, J.A., Turnbull, S.J. et al. (2015) A geophysical strategy for measuring the thickness of the critical zone developed over basalt lavas. *Geosphere*, 11(2), 514–532. Available from: https://doi.org/10.1130/GES01142.1

Zelt, C.A. (1999) Modelling strategies and model assessment for wide-angle seismic traveltime data. *Geophysical Journal International*, 139(1), 183–204. Available from: https://doi.org/10.1046/j.1365-246X.1999.00934.x

Zelt, C.A. & Smith, R.B. (1992) Seismic traveltime inversion for 2-D crustal velocity structure. *Geophysical Journal International*, 108(1), 16–34. Available from: https://doi.org/10.1111/j.1365-246X.1992.tb00836.x

**How to cite this article:** Trichandi, R., Bauer, K., Ryberg, T., Scherler, D., Bataille, K. & Krawczyk, C.M. (2022) Combined seismic and borehole investigation of the deep granite weathering structure—Santa Gracia Reserve case in Chile. *Earth Surface Processes and Landforms*, 47(14), 3302–3316. Available from: https://doi.org/10.1002/esp.5457